Journal of Biomechanics 90 (2019) 40–49

Contents lists available at ScienceDirect

Journal of Biomechanics

journal homepage: www.elsevier.com/locate/jbiomech
www.JBiomech.com

Tomographic PIV in a model of the left ventricle: 3D flow past biological and mechanical heart valves

Hicham Saaid [a], Jason Voorneveld [b], Christiaan Schinkel [c], Jos Westenberg [d], Frank Gijsen [b], Patrick Segers [a], Pascal Verdonck [a], Nico de Jong [b], Johan G. Bosch [b], Sasa Kenjeres [c], Tom Claessens [e]

[a] Institute Biomedical Technology, Ghent University, Ghent, Belgium
[b] Department of Biomedical Engineering, Thoraxcenter, Erasmus MC University Medical Center, Rotterdam, the Netherlands
[c] Department of Chemical Engineering, Faculty of Applied Sciences, Delft University of Technology, Delft, the Netherlands
[d] Department of Radiology, Leiden University Medical Center, Leiden, the Netherlands
[e] Department of Materials, Textiles and Chemical Engineering, Ghent University, Ghent, Belgium

ARTICLE INFO

Article history:
Accepted 15 April 2019

Keywords:
Particle image velocimetry
Tomographic PIV
Left ventricle
Flow
Prosthetic heart valves

ABSTRACT

Left ventricular flow is intrinsically complex, three-dimensional and unsteady. Its features are susceptible to cardiovascular pathology and treatment, in particular to surgical interventions involving the valves (mitral valve replacement). To improve our understanding of intraventricular fluid mechanics and the impact of various types of prosthetic valves thereon, we have developed a custom-designed versatile left ventricular phantom with anatomically realistic moving left ventricular membrane. A biological, a tilting disc and a bileaflet valve (in two different orientations) were mounted in the mitral position and tested under the same settings. To investigate 3D flow within the phantom, a four-view tomographic particle image velocimetry setup has been implemented. The results compare side-by-side the evolution of the 3D flow topology, vortical structures and kinetic energy in the left ventricle domain during the cardiac cycle. Except for the tilting disc valve, all tested prosthetic valves induced a crossed flow path, where the outflow crosses the inflow path, passing under the mitral valve. The biological valve shows a strong jet with a peak velocity about twice as high compared to all mechanical heart valves, which makes it easier to penetrate deeply into the cavity. Accordingly, the peak kinetic energy in the left ventricle in case of the biological valve is about four times higher than the mechanical heart valves. We conclude that the tomographic particle imaging velocimetry setup provides a useful ground truth measurement of flow features and allows a comparison of the effects of different valve types on left ventricular flow patterns.

1. Introduction

The left ventricle (LV) is believed to preserve the momentum of the incoming blood flow during diastole by keeping it in motion during diastasis and smoothly redirecting it towards the outflow tract during systole (Kim et al., 1995; Kilner et al., 2000). The topology of these flow structures is determined by the geometry of the LV cavity, the morphology of the mitral valve and the electrical conduction system (Bermejo et al., 2015; Mele et al., 2018). Various multidisciplinary studies have been conducted to better understand the pathophysiology of heart disease, to define clinically useful indicators of cardiac function (Gharib et al., 2006; Belohlavek, 2012) and/or to understand the effect of mitral valve repair or replacement by a prosthetic device on the LV flow (V Vraghav , Sudeep Sastry, 2018). The choice of a biological vs. mechanical prosthesis for instance is still an open debate (Chikwe, 2018) as shown in a recent observational study by (Goldstone, 2017).

Particle image velocimetry (PIV) has been extensively used to study the effect of different prosthetic valves on the LV flow pattern (Pierrakos et al., 2004; Kheradvar et al., 2006; Querzoli and Fortini, 2010; Falahatpisheh and Kheradvar, 2012; Vukićević et al., 2012; Wang et al., 2017). A common limitation of these PIV studies is their 2D approach, yielding an incomplete view of the inherently three-dimensional (3D) flow structures in the LV and the inability to calculate all nine components of the velocity gradient tensor. There have been various attempts to overcome this limitation by reconstructing the 3D velocity vector field in the whole LV from velocity data obtained from separate measurement planes. The latter are either two-component velocity (Fortini et al., 2013; Falahatpisheh et al., 2014) or three-component velocity data, obtained by the stereoscopic PIV technique (Tan et al.,

https://doi.org/10.1016/j.jbiomech.2019.04.024
0021-9290/

2016; Saaid et al., 2018). Both reconstructive methods take advantage of the periodicity of the cardiac cycle but require complex setups to translate or rotate the PIV system as well as time-consuming calibration and/or post processing procedures.

Tomographic PIV (Tomo-PIV) is considered the first "true" volumetric PIV technique (Elsinga et al., 2005). In contrast to traditional planar PIV techniques, Tomo-PIV allows instantaneous extraction of all three velocity components over the entire volume of interest. To date, Tomo-PIV has been used for studying the blood flow in the aortic root (Hasler et al., 2016; Hasler and Obrist, 2018), the carotid artery (Buchmann et al., 2011) and the intracranial aneurysm (Roloff et al., 2018).

Considering the above, the goal of the following work is twofold. First, we aim to demonstrate the feasibility of a tomographic, full-volumetric PIV technique to capture the 3D flow in a realistic and compliant LV model. Additionally, this phantom is compatible with 3D ultrasound and MRI imaging, such that 3D flow measurements acquired by these in-vivo medical imaging approaches can be compared to the optical ground truth in the future. Second, we compare the flow field generated by three structurally different prosthetic heart valves (biological, tilting disc and bileaflet) under the same running conditions.

2. Materials and methods

2.1. Left ventricle membrane and tank

An optically transparent compliant silicone LV replica (0.5 mm thick) (Fig. 1b) was manufactured by painting four layers of silicone (HT 33 Transparent LT, Zhermack SpA, Rome, Italy) onto a 3D printed LV mould (Fig. 1a). The shape of the LV mould was extracted from the statistical mean of a dataset of segmented 4D computed tomography images of 150 patients (Kirişli et al., 2010; Metz et al., 2012; Voorneveld et al., 2018). The silicone has a refractive index of 1.413, measured by an Abbe refractometer (Bleeker, Zeist Holland).

The LV membrane was connected to the valve holders (Fig. 1c), and immersed (Fig. 1d) in a Plexiglas nine-sided polygon tank (Fig. 2a). The Plexiglas plates were machined and then glued together using a two-component reaction adhesive (Acrifix 192, Evonic Industries). Fig. 2a depicts the LV flow loop, which consists of a pressurized aortic chamber and an atrial chamber kept at atmospheric pressure. The outlet from the aortic chamber is connected to the left atrial chamber via an adjustable peripheral resistance valve (Vivitro Labs Inc., Victoria, BC, Canada) with a short length of silicone rubber hose.

2.2. Hydraulic circuit

A pulsatile pump (Vivitro Labs Inc., BC, Canada) was used to mimic the pumping action of the LV. The hydraulic piston pump was connected to the acrylic tank (Fig. 2a) with semi-rigid tubing. The pump was velocity-controlled and set to generate a sinusoidal-like waveform with a frequency of 70 beats per minute and a duty cycle of 35%, resulting in a 300 ms systolic period and a stroke volume of 50 ml. Pressure transducers (6069, Utah Medical Products, Inc., Athlone, Ireland) were used to monitor the pressure in the aorta and inside the tank.

2.3. Imaging system and illumination

The imaging system consists of two high-speed cameras (Imager Pro HS 4 M, PCO, Kelheim, Germany) set to record at 2000 fps. The setup was primarily designed to perform tomographic PIV from four different viewing angles using two cameras (Fig. 3a). For this purpose, a custom-made image splitter (consisting of 8 first surface mirrors) has been placed in front of each camera (Fig. 3a). Macro prime lenses with a focal length of 100 mm (Samyang Optics co Ltd., Korea) were used. A long-pass filter at 540 nm (Thorlabs, Inc., Newton, NJ, USA) was mounted in front of each lens to selectively capture the scattered fluorescent particle light. A volume of approximately $80 \times 110 \times 70\ mm^3$ was illuminated by a double-cavity pulsed Nd:YLF laser (527 nm Litron Laser, England). Diverging lenses were used to shape the laser beam into a full-volume illumination.

2.4. Working fluid and tracer particles

A two-component working fluid was chosen to match the measured refractive index (1.4130) of the LV silicone membrane, thereby minimizing optical distortion. The ratio of the components in the fluid mixture (60% glycerol and 40% distilled water) was adjusted until its measured refractive index (1.4140) very closely matched that of the silicone. The dynamic viscosity and density of the working fluid were 17.7 mPa·s and 1160 kg/m^3, respectively. Fluorescent Rhodamine-B coated particles with a diameter of 20–50 μm and density of 1100 kg/m^3 were used as tracers.

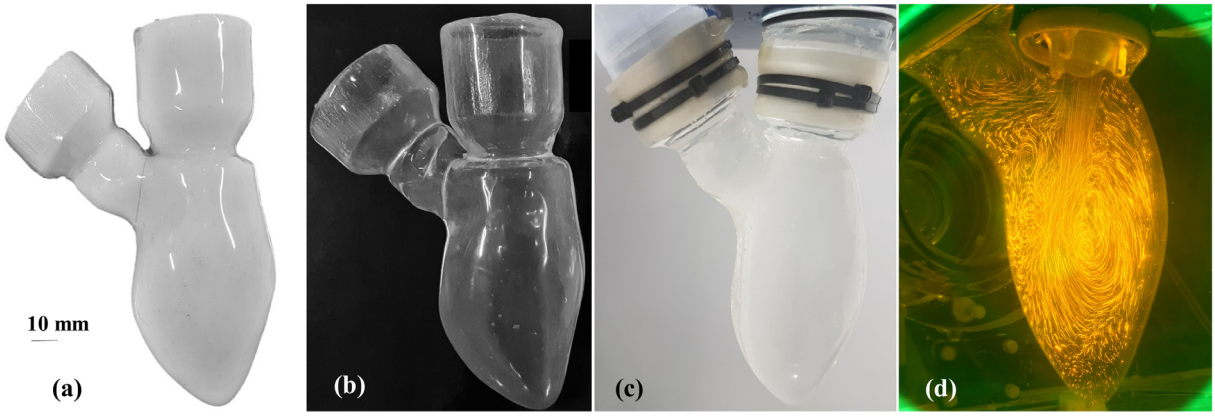

Fig. 1. (a) 3D-printed LV mould representing *the endocardial shape at end systole,* fitted with a mitral inflow and aortic outflow tract. (b) LV silicone membrane. (c) LV model attached to valve holders using cable ties. The outflow tract is tilted about 40° with respect to the mitral valve axis. (d) A long exposure picture of fluorescent particles within the LV.

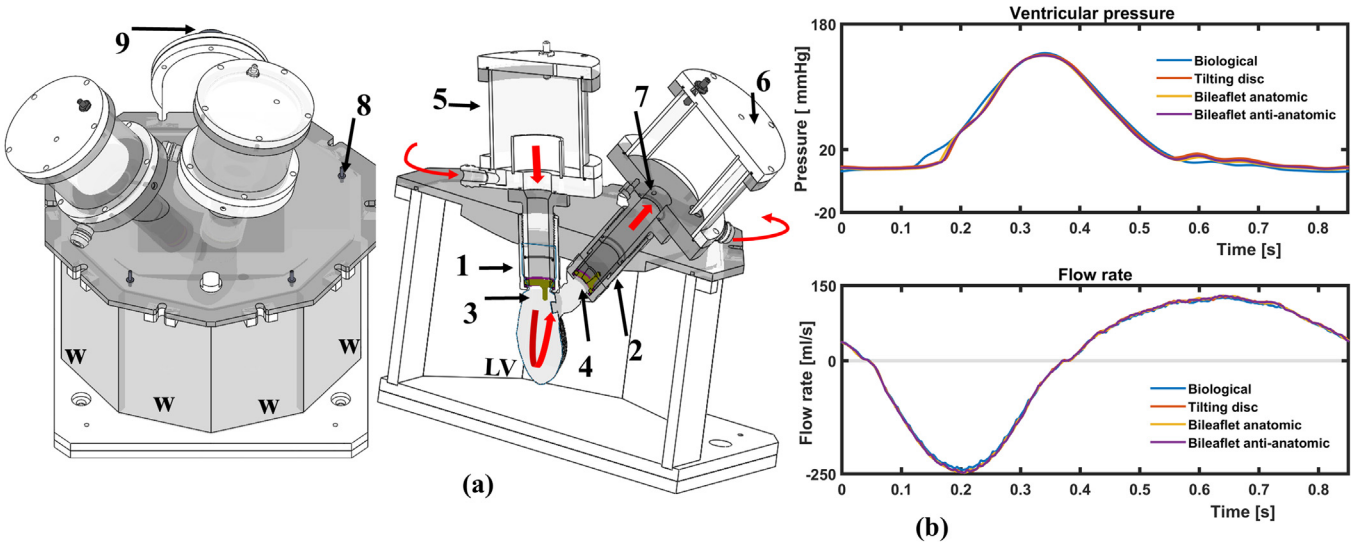

Fig. 2. (a) CAD view of the nine-sided tank. The shape of the tank provides undistorted optical access to the LV from different angles. *W indicates the four windows used for optical access. The red arrows depict the LV flow loop.* 1–2: valve holders, 3–4: mitral and aortic valve position, 5–6: atrial and aortic blocks, 7: aortic pressure catheter, 8: multiple hose connectors for air removal and ventricular pressure monitoring, 9: pump connector. (b) Representative samples of ventricular pressure recorded during the PIV experiments and flow waveforms imposed at the pump. (For interpretation of the references to colour in this figure legend, the reader is referred to the web version of this article.)

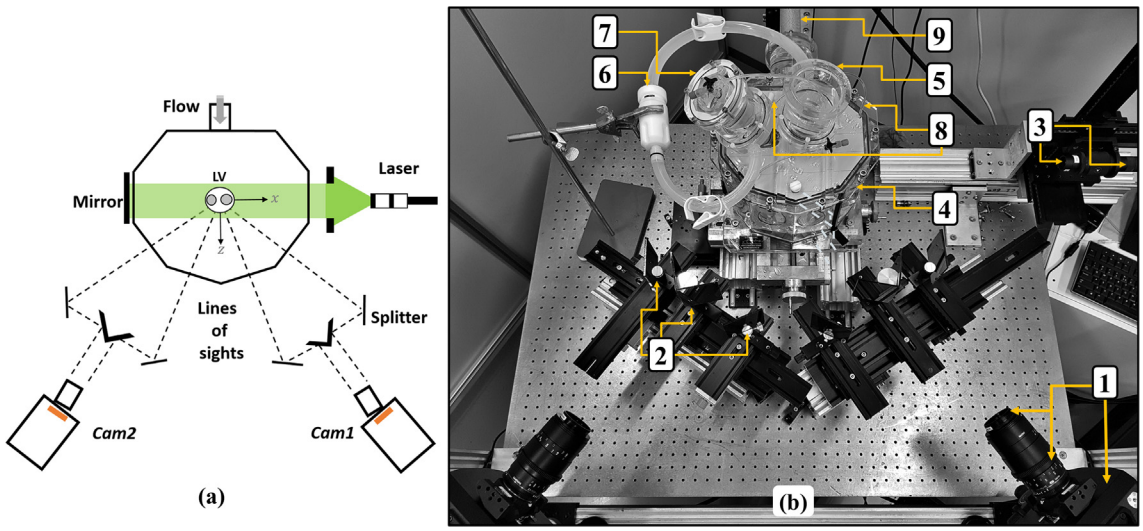

Fig. 3. (a) Schematic sketch (top view) of the tomo-PIV setup. (b) Picture of tomo-PIV setup in linear configuration with two high-speed cameras equipped with prime lenses and filter (1), two mirror splitter system (2) and laser arm with telescopic head and optics compound (3). The nine-sided tank (4), with atrial (5) and aortic blocks (6), connected with peripheral resistance (7). Pressure transducer tubes (8). The tank is connected to the pulsatile pump via a semi-flexible tube (9).

2.5. Calibration

A two-level calibration target was placed with a micrometre stage in nine positions equally spaced over 40 mm in the tank (without the LV membrane). To map the 3D space object onto the 2D camera sensor plane, a third-order polynomial fitting method was applied. The geometrical calibration yielded an average error for all cameras and views of approximately 0.2 pixel. Subsequently, an ensemble of 200 particle images has been acquired to perform the iterative volume self-calibration procedure (Wieneke, 2008). After four iterations, the volume self- calibration was able to reduce the disparity to less than 0.02 pixels for all cameras.

2.6. Tomographic analysis

All particle images were pre-processed to remove background intensity with a 7×7 sliding minimum kernel. Due to the Gaussian laser illumination shape, an intensity normalization filter was applied. Subsequent image processing involves 3×3 Gaussian smoothing, successive sharpening and manually masking out the non-flow regions. Following the suggested particle concentration from literature (Scarano, 2012) a concentration of 0.04 particles per pixel (PPP) was reached as an optimal measurement condition. The time separation Δt of 500 μs between image pairs was optimized to ensure that maximum particle displacement is about 6–10 pixels. All tomographic PIV data were processed with Davis 10 (LaVision, Göttingen, Germany).

2.7. Measurement protocol

The measurements were performed within the LV with three different heart valves mounted in the mitral position (Fig. 4a): a 25 mm tricuspid biological, a 24 mm tilting disc and a 25 mm Bicarbon bileaflet valve which was mounted in two different orien-

tations (anatomic and anti-anatomic). In all series a 19 mm Perimount Magna Ease (Edwards Lifesciences) tricuspid biological valve was used as an aortic valve. The particle images were reconstructed at 61 time points over the cardiac cycle (temporal resolution of 14 ms). The data from ten cardiac cycles were phase-averaged for each heart valve configuration. Table 1, summarizing the relevant setup and processing parameters, is provided as a supplementary material.

3. Results and discussion

In the following, the Tomo-PIV phase-averaged velocity data are presented. The first subsection illustrates the mean flow velocity field downstream of the four prosthetic valves. Further, we focus on the inflow characteristics by comparing the flow rate through transversal slices over time. In the last two subsections, we present the vortical structures and kinetic energy computed in the entire LV domain.

Fig. 4b compares the maximum inlet flow velocity between the four valves. The biological valve (BHV) opens slightly later than the mechanical valves (MHVs) and the transmitral flow velocity increases more rapidly for the BHV, reaching a peak value of up to 1 m/s – twice the magnitude of the MHVs. At the onset of the diastole, the tilting disc produces slightly higher velocities than the two bileaflet configurations. The two orientations of the bileaflet valve yielded virtually identical inlet velocities throughout diastole.

3.1. Flow velocity field

A note of caution is necessary, because of the large difference in the flow velocity range between the biological and mechanical valves (Fig. 4b), different colour scales were used for the *iso*-surfaces and velocity maps (Fig. 5). Fig. 5 shows the mean flow topology of the tested heart valves (indicated with letters) at four characteristic phases (indicated with Roman numerals) during the cardiac cycle. The flow topology is represented by means of *iso*-surfaces based on the velocity magnitude and cross-sectional slices coloured with axial velocity.

Biological valve: Initially, a strong transmitral jet is directed towards the anterior LV wall (time steps I–II). By the end of diastole (time step III), the inner core of the inflow starts disappearing (high velocity isosurface). Further, the inflow swirls towards the posterior wall, forming a counter-rotating flow pattern occupying the entire cavity. This flow feature is believed to prevent blood stasis by washing-out the apical region. The outgoing flow slides along the posterior wall and then crosses the inflow tract (time step IV). The crossed flow path shown here with the BHV (dashed line Fig. 5) agrees with previous in vivo studies (Pierrakos et al., 2004; Faludi et al., 2010; Pedrizzetti et al., 2010; Akiyama et al., 2017; Nakashima et al., 2017), where the flow passing the BHV was shown to generate a strong jet towards the intraventricular septum and then to cross the inflow path (i.e. passing under the mitral valve) during systole (Fig. 5a).

Monoleaflet valve: At the onset of the filling phase (time step I) the valve induces a primary jet passing the main orifice. The primary jet advances along the posterior wall, while a secondary jet passes from the anterior orifice towards the anterior wall (time step II). At the end of diastole, the incoming flow forms a clockwise large-scale vortex (time step III) that is smoothly redirected towards the outflow tract. This looped flow path is in concordance with previous 2D-PIV investigations (Cenedese et al., 2005; Vukićević et al., 2012; Voorneveld et al., 2018; Khalafvand et al., 2018).

Bileaflet valve: The two valve orientations exhibit minor differences in flow topology at the onset of the filling phase (Fig. 5c and d): in both cases the jet emanating from the outer orifices is significantly stronger than in the central orifice (time steps I–II). In the anatomic configuration (Fig. 5c), the jet on the anterior wall septum rolls off under the aortic valve, whereas due to the "Coanda effect" the opposite jet tends to realign with the central inflow jet (time steps II–III). In the anti-anatomic orientation (Fig. 5d), on the other hand, the flow pattern through the outer orifices appears to be nearly symmetric (time steps II–III). In both configurations, at mid diastole the strong central jet merges with the outer jets towards the apex. The *iso*-velocity surface emanating from the mitral valve dissipates before reaching the apex (Fig. 5c and d), as

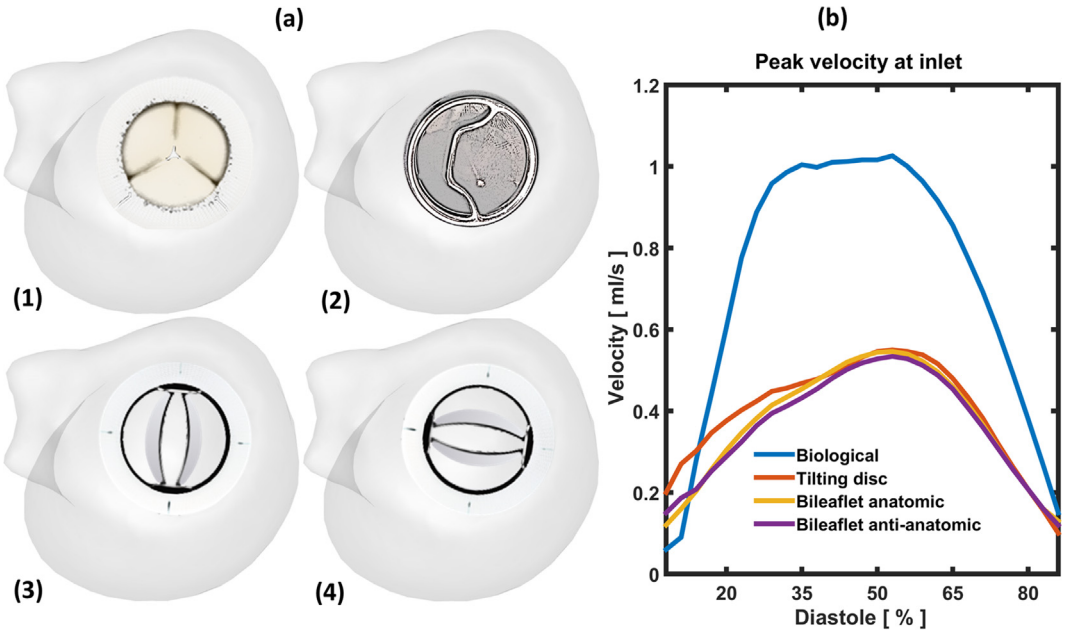

Fig. 4. (a) Snapshots of the LV model and heart valves in the mitral position: (1) biological Perimount 2900 (Edwards Lifesciences, Irvine, USA); (2) tilting disk (Björk-Shiley); (3–4) bileaflet (Sorin Biomedica, Saluggia, Italy) in anatomic and anti-anatomic orientation, respectively. (b) peak velocity of the inflow jet during the diastolic phase.

Table 1
An overview on the most important parameters for the PIV system, hydraulic setup and tomographic PIV analysis.

Imaging	Camera[a]	CMOS sensor
	Resolution and dynamic range	2016 × 2016 pixel, 12bit
	Pixel size	11 μm
	Acquisition rate[b]	2 kHz
	Exposure time	20 μs
	Lens focal length[c]	100 mm
	Lens aperture[d]	16
	Field of view	70 × 100 × 60 mm^3
	Max. particle displacement	6–10 pixel
	Digital image resolution	12.4 pixel/mm
Laser	Type	Nd:YLF
	Pulse width	~100 to 150 ns
	Pulse distance	200 μs
	Volume illumination[e]	80 × 110 × 70 mm^3
	Total laser energy	44 mJ at 2 kHz
	Illuminated volume	90 × 110 × 65
Seeding	Type	Rhodamine-B
	Diameter	20–50 um
	Density	1100 kg/m^3
Fluid	Mixture	60% glycerine, 40% water
	Refractive index	1.413
	Density	1160 kg/m^3
	Dynamic viscosity	17.7 mPa·s
Prosthetic valves	Aortic Mitral	Biological tricuspid 19 mm Biological tricuspid 25 mm Bileaflet curved leaflet 25 mm Tilting disc 24 mm
Flow parameters	Heart frequency	70 BPM
	Stroke volume	50 ml
	Peak LV pressure	150 mmHg
	Peak aortic pressure	150 mmHg
Tomo-PIV	Volume size	62 × 100 × 57 mm (x,y,z) 760 × 1226 × 699 voxels
	Particle density	0.04 PPP
	Physical calibration[f]	Two-level
	Volume self-calibration[g]	0.2 pixel (average error) 0.02 pixel
	N° of iterations	8
	Correlation	96–48 voxels
	N° of passes	4
	Overlap factor	75%
	Spatial resolution	0.98 mm
	N° of vectors	63 × 102 × 58

Practical notes on the PIV setup and post processing

[a] To minimize the vibrations transmitted to the imaging system, the cameras were mounted on a tripod head with a load capacity of 12 kg (3D Super Pro 3-way, Manfrotto, Italy) and fixed on rigid optical rails screwed to an optical table (Thorlabs, Inc., Newton, NJ, USA).

[b] After cropping the sensor to the region of interest

[c] The lenses were mounted on tilt adapters, which allows to meet the Scheimpflug criterion (Zang and Prasad, 1997).

[d] To be able to cover the whole measurement domain and to avoid the particle blurring effects due to limited depth of field, an aperture of f/16 has been set.

[e] To create homogeneous illumination, a mechanical mask has been placed in front of the laser arm (Fig. 3b). With the aim to increase the light intensity, the laser light was recycled by placing a mirror on the opposite side of the column.

[f] A two level calibration plate with circular markers (distributed uniformly with an interval of 10 mm) has been used.

[g] Prior to the self-calibration, the images were pre-processed by a history-minimum-background subtraction (Scarano, 2012) and intensity normalization. The volume domain has been subdivided in 8 × 8 × 5 sub-volumes. In the first step, the averaged disparity vector magnitude was about 0.5 pixel.

previously described in (Pierrakos et al., 2004). Additionally, our results indicate that in both configurations the bileaflet valve gives rise to a crossed flow path. This confirms the findings from a prior in vivo study from (Faludi et al., 2010). Conversely, (Nakashima et al., 2017), using an ultrasound based vector flow mapping technique, showed that only the anti-anatomical orientation is associated with a crossed flow path. In our previous work (Saaid et al., 2018), we even observed that both orientations lead to a looped flow path. Some of the discrepancies may be due to the highly simplified LV shape and the different LV diameter/valve ratio (Saaid et al., 2018) or a limitation of two-dimensional echocardiography in case of (Nakashima et al., 2017). Movie 1 (online supplement) depicts the flow field throughout one cardiac cycle for each valve model.

3.2. Inflow characteristics

For a more quantitative comparison between the BHV and the MHVs, the volume flow rate has been calculated through four cross-sections (Fig. 6) over one cardiac cycle. As shown in Fig. 6 (cross-section 1), the three mechanical valves open simultaneously. The two bileaflet orientations behave similarly in the first slices with a slightly higher flow rate than the biological and the tilting disc valves during the diastole. Moving towards the apex, in cross-sections 3 and 4, the penetration depth of the jet decreases drastically in the MHVs. In fact, the BHV exhibits a much higher downward flow over the filling phase compared to the bileaflet valve in anatomic configuration (cross-section 4). The stagnation phenomena in a LV have also been reported in a 2D-PIV investigation by Faludi and co-workers (Faludi et al., 2010), showing that the jet entering the LV cavity collides more closely to the apex with a biological valve than with a bileaflet valve. Compared to the MHVs, the inflow jet through the BHV is more likely to reach and wash out the apical region. This potentially avoids stagnation zones and reduces the risk for thrombosis formation. In patients with dilated cardiomyopathy or myocardial infarction, where abnormal flow patterns are known to promote blood stasis between the apex and outflow tract (Dantzig, 1995; Sengupta et al., 2008; Hendabadi et al., 2013), we would expect the BHV to perform better than the MHVs.

3.3. Vortical structures

The lambda-2 (λ_2) method has been used to identify the 3D vortical flow features over the cardiac cycle (Jeong and Hussain, 1995). In Fig. 7, one can clearly see the formation of the vortex rings (time step I) and observe how they elongate, propagate and then dissipate during diastole. The strong inflow through the biological valve develops as a single vortex ring in the shear layer around the incoming jet (time steps I–II–III). The primary vortex ring is connected to a secondary vortex via branched tubes (trailing vortex tubes). The two vortices travel towards the mid-ventricle and start to break down in small structures before reaching the apex. The described vortex ring formation downstream the BHV is somewhat similar to the vortices generated from a cylinder with an inclined exit (Troolin and Longmire, 2010). Comparable flow structures have also been described in previous LV fluid dynamic simulations (Watanabe et al., 2008; Le and Sotiropoulos, 2012; Khalafvand et al., 2019) and in vivo studies (Elbaz et al., 2014).

The three MHVs exhibited different vortical flow features compared with the BHV. In case of the tilting disc, the flow through the posterior orifice yields a strong shear layer and interacted with the boundary layer along the lateral wall generating a curved vortex ring (Fig. 7b). The vortical structures then shed from the valve leaflets, progress toward the mid regions, and finally dissipate by the end of the diastole due to viscous interaction with the ventricular wall.

Due to the leaflet geometry of the bileaflet valve, the inflow is spread over multiple orifices, rendering the formation of a single

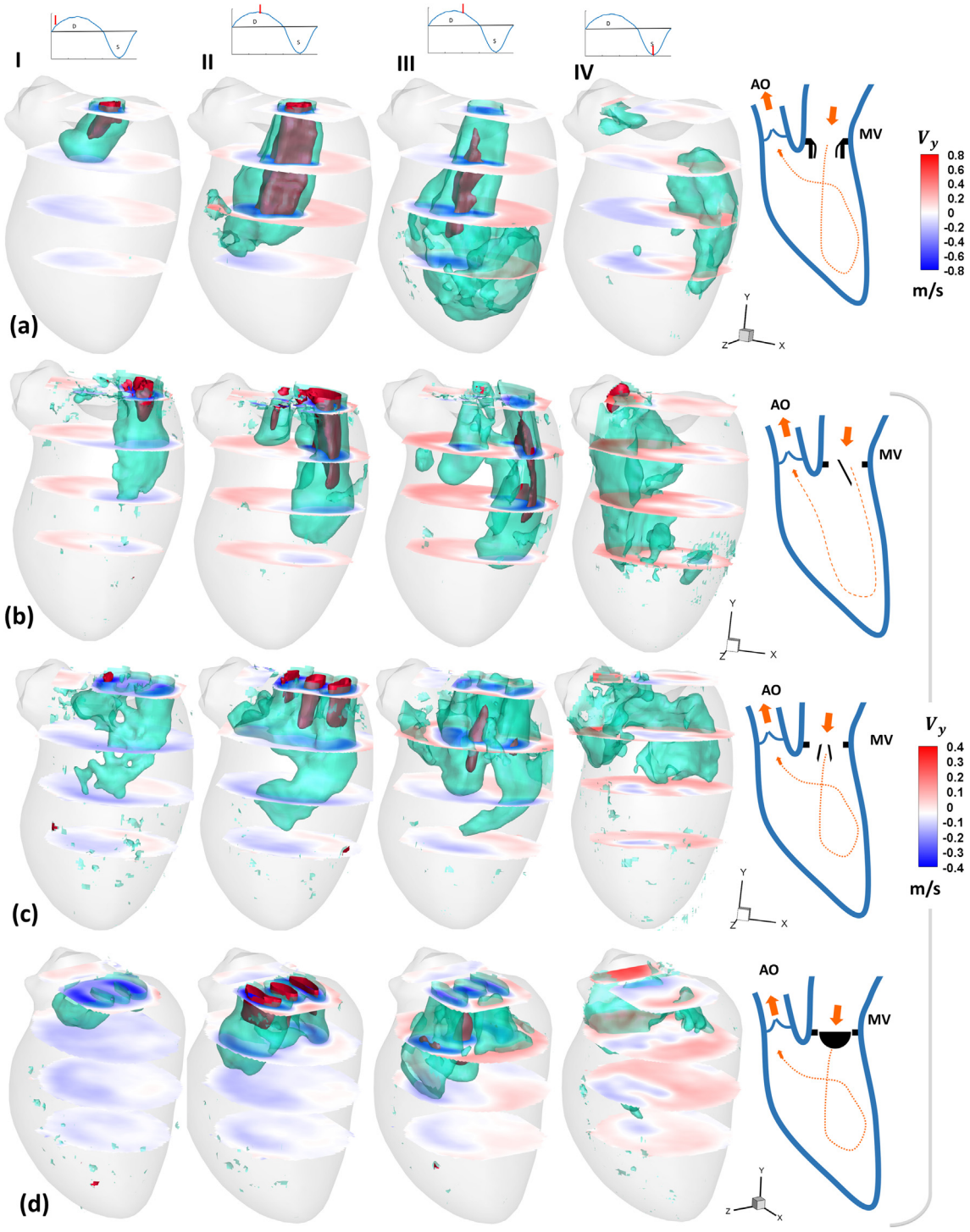

Fig. 5. Time-sequence of the mean flow structures downstream of the mitral valves: (a) biological, (b) tilting disc, and bileaflet in (c) anatomic and (d) anti-anatomic orientation. Note that (d) is slightly rotated about the y-axis to improve visibility of the flow structures. Two *iso*-velocity surfaces are shown for each valve (at 0.35 m/s and 0.75 m/s in case of the BHV and at 0.15 m/s and 0.35 m/s in case of the MHVs). *On the right, a sketch of the LV and prosthetic valve showing the flow path (looped or crossed) with a dashed line*. The cross-sections are colour-coded based on the axial velocity (v_y). Roman numerals indicate the time steps (I = 0.35 s, II = 0.55 s, III = 0.8 s, IV = 0.2 s).

vortex impossible. Thus, the bileaflet valve induces incomplete vortex rings through the three orifices (Fig. 7c and d). At the onset of the filling phase, the flow is dominated by tubular structures generated from the outer orifices. Further into diastole (time step IV), a jet is formed from the central orifice with higher propagation velocity, forming a concentric coherent structure. The latter interact rapidly with each other and with the surrounding LV wall, disintegrating into smaller flow structures. Additionally, the so-called vortex ring was observed only downstream the biological valve with the formation of multiple vortex rings. The complete evolu-

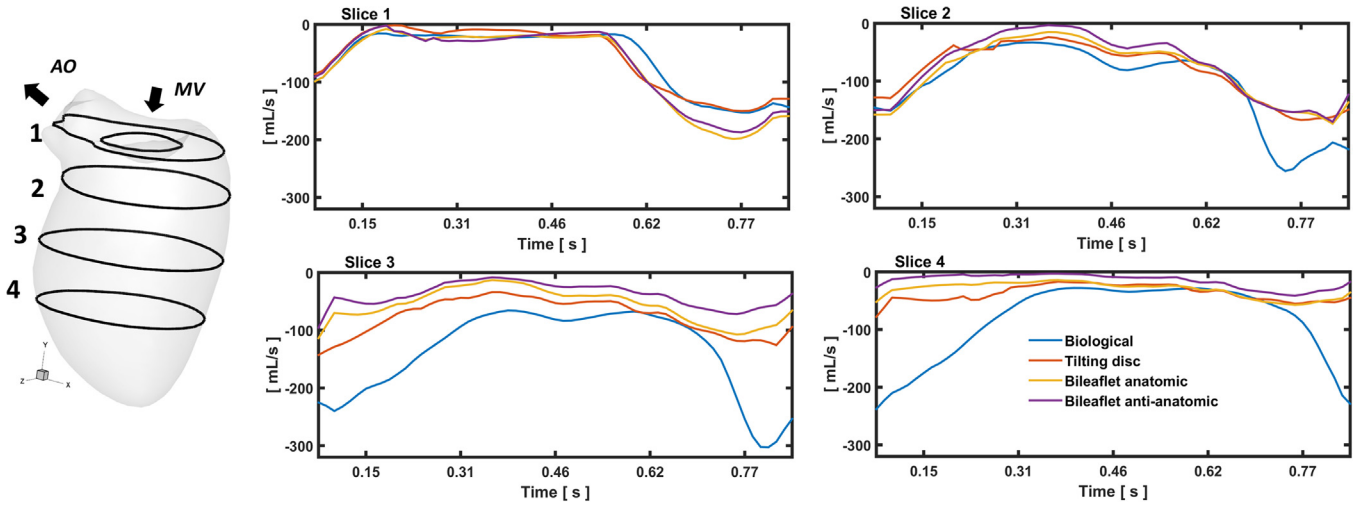

Fig. 6. Left: Four equidistant (20 mm) cross-sections within the LV model. The first slice is positioned approximately 5 mm below the mitral valve. Right: Volume flow rate computed through four cross-sections for each valve. Only the downward flow was considered; velocities with a positive sign (v_y) were blanked. The MHVs open approximately at 0.54 s whereas the biological open at 0.58 s.

tion of the vortical flow structures past the prosthetic heart valves over the cardiac cycle is provided as a supplementary material (Movie 2).

3.4. Kinetic energy

The time course of integral kinetic energy (KE) computed for the entire LV domain is shown in Fig. 8. The peak value of the kinetic energy passing the BHV is approximately four times higher than for the MHVs, as could be expected from the two-fold difference in the velocity magnitude profile during the cardiac cycle (Fig. 4). A significant difference in terms of KE between BHV and bileaflet valve has been also reported in a recent numerical study by (Meschini et al., 2018). All mechanical valves exhibit a similarly shaped KE profile throughout the cardiac cycle. The tilting disc lead to higher KE levels during mid diastole and systole than did the bileaflet valve. In case of the bileaflet valve, the anatomic orientation yielded a slightly higher KE than the anti-anatomic configuration.

3.5. Limitations

Despite the aforementioned advantages of the employed technique, some limitations are worthwhile mentioning. Tomo-PIV hardware and software are generally more complex and expensive than 2D PIV or multiplane scanning setups. However, to reduce the cost of the PIV apparatus, a four-view Tomo-PIV imaging system has been implemented using a combination of only two cameras (instead of four) and a mirror system. Also, while Tomo-PIV does not require physical alignment between illumination and the calibration target, it is more sensitive to vibrations compared to stereoscopic PIV, which may lead to camera misalignment during the acquisition. To overcome this, we followed a well-established procedure for physical calibration, followed by the volume-self calibration. Due to computational cost and amount of data storage, we have presented only the averaged flow field data based on 10 cycles. A semi-quantitative convergence analysis (consisting of a comparison between the phase averaged data obtained from 10, 20 and 30 cycles) showed no discernible difference between 20 and 30 cycles. Only at peak early inflow a 7% difference in flow velocity was found between the results obtained with 10 cycles and the converged flow velocity data using 30 cycles. Moreover, we would like to mention that more advanced Lagrangian software algorithms, such as Shake-The-Box (Schanz et al., 2016), may be more appropriate to analyse the time-resolved data in the future. Furthermore, the piston pump was driven by a sinusoidal-like wave form that does not represent diastasis and the late filling (A-wave). Consequently, it was not possible to investigate the interaction between the flow structures induced at the early filling and the fresh fluid entering during the late filling wave, as described in vivo (Elbaz et al., 2014) and in a recent numerical simulation study (Khalafvand et al., 2018), using a similar LV geometry and a more realistic flow waveform. Also, the working fluid mixture has a dynamic viscosity four times higher than blood, which may have affected the flow resistance and consequently the formation and viscous dissipation rate of the vortical structures.

4. Conclusion

This work demonstrated the feasibility and usefulness of tomographic PIV, to study 3D flow dynamics in a compliant model. To the best of our knowledge, this study provides the first tomographic PIV study of the 3D flow pattern in a flexible left ventricular shape membrane, downstream of biological and mechanical valves.

We have analysed the effect of three types of prosthetic mitral heart valves on intraventricular flow under the same hydraulic conditions. The qualitative and quantitative flow analyses suggest that the biological valve generates flow patterns similar to those observed in vivo after a BHV valve replacement. Except for the tilting disc, all tested prosthetic valves induced a crossed flow path, where the outflow crosses the inflow path, passing under the mitral valve. Further, the inflow jet in the BHV penetrated deeper into the LV cavity compared to the MHVs. The lambda-2 method for vortex identification showed the formation of multiple vortex rings in the presence of the BHV. The kinetic energy level associated with the BHV during diastole is approximately four times higher than the MHVs. Finally, we showed that the anatomic orientation of the bileaflet valve yields an overall slightly higher kinetic energy than the anti-anatomic configuration. Yet, none of our performed analyses reveal that one orientation of the bileaflet valve is to be preferred over the other.

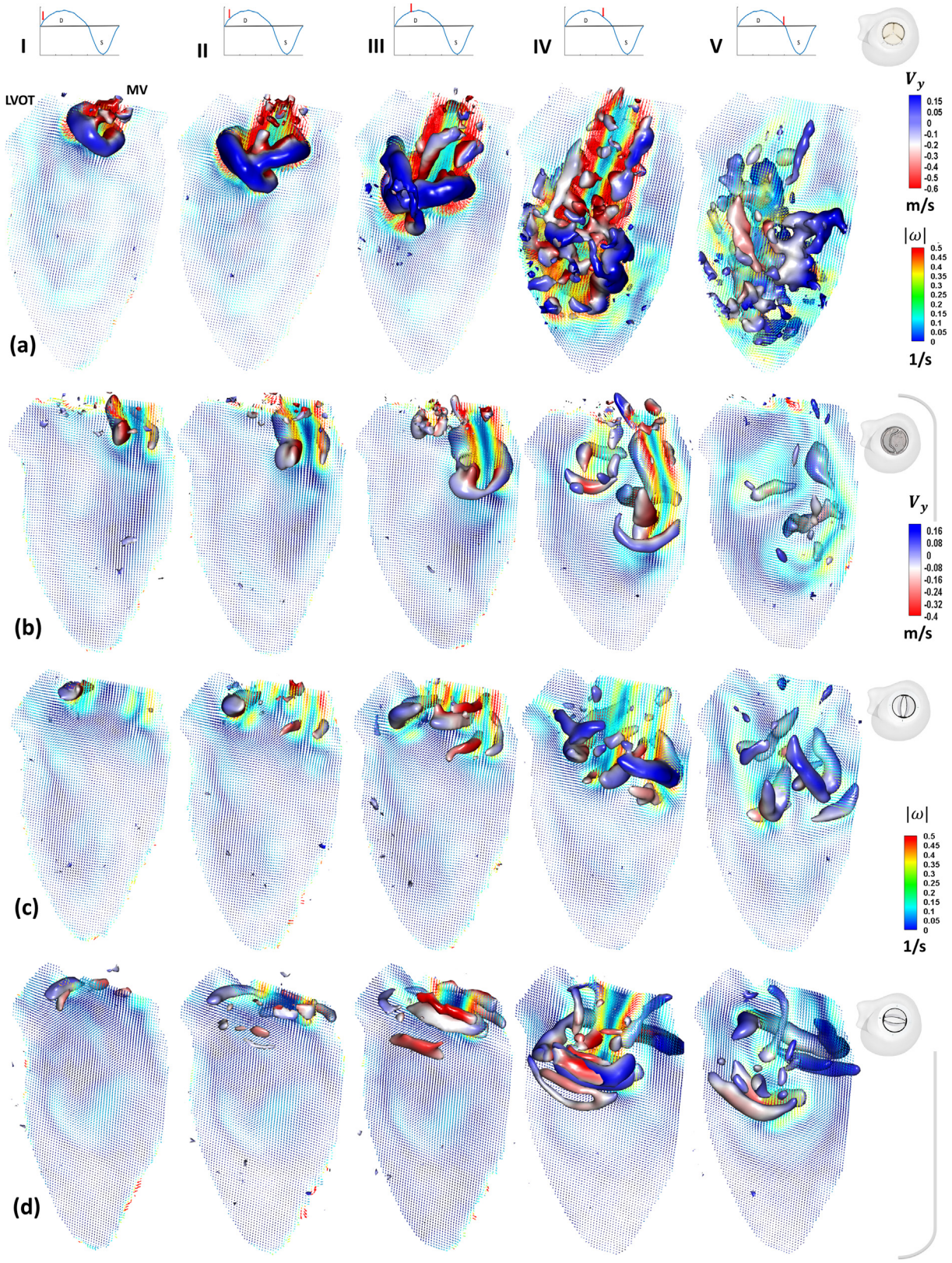

Fig. 7. 3D vortical structures recognized by lambda-2 method are visualized as *iso*-surface ($\lambda_2 = -0.015$) and colour-coded with the axial velocity component. The 2D velocity vector field maps are coloured based on vorticity magnitude. (a) Biological, (b) tilting disc, and bileaflet in anatomic (c) and anti-anatomic (d) orientation. Roman numerals indicate the time steps (I = 0.35 s, II = 0.45 s, III = 0.55 s, IV = 0.65 s, V = 0.85 s).

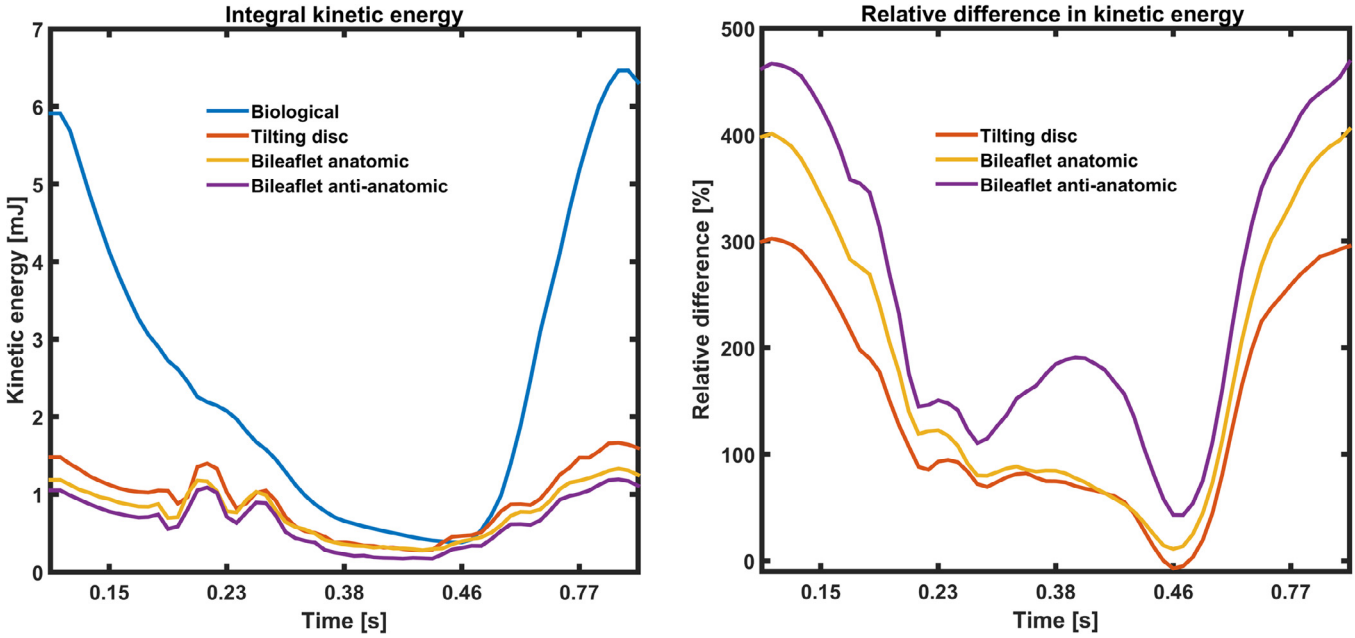

Fig. 8. Left: the evolution of the kinetic energy within the LV domain, computed over the cardiac cycle as: $KE = 0.5\rho \int V^2 dv$, where $\rho = 1060 kg/m^3$ and V is velocity magnitude. *Right: The difference of KE in the biological valve relative to each of the mechanical valves, calculated as:* $100\% * (BHV - MHV_i)/MHV_i$

Acknowledgements

We acknowledge Michiel Manten and Geert Springeling of Erasmus Medical Center, for their assistance in fabricating the phantom. This work was supported in part by ZonMw within the Innovative Medical Devices Initiative (IMDI), Netherlands program (project Heart Failure and 4D Flow)

Conflict of interest statement

All authors declare that there are no conflicts of interest.

Appendix A. Supplementary material

Supplementary data to this article can be found online at https://doi.org/10.1016/j.jbiomech.2019.04.024.

References

Akiyama, K., Nakamura, N., Itatani, K., et al., 2017. Flow-dynamics assessment of mitral-valve surgery by intraoperative vector flow mapping. Interact. Cardiovasc. Thoracic Surg. 24, 869–875. https://doi.org/10.1093/icvts/ivx033.

Belohlavek, M., 2012. Vortex formation time: An emerging echocardiographic index of left ventricular filling efficiency? Eur. Heart J. Cardiovasc. Imag. 13, 367–369. https://doi.org/10.1093/ejechocard/jer311.

Bermejo, J., Martínez-Legazpi, P., del Álamo, J.C., 2015. The clinical assessment of intraventricular flows. Annu. Rev. Fluid Mech. 47, 315–342. https://doi.org/10.1146/annurev-fluid-010814-014728.

Buchmann, N.A., Atkinson, C., Jeremy, M.C., Soria, J., 2011. Tomographic particle image velocimetry investigation of the flow in a modeled human carotid artery bifurcation. Exp. Fluids 50, 1131–1151. https://doi.org/10.1007/s00348-011-1042-1.

Cenedese, A., Del Prete, Z., Miozzi, M., Querzoli, G., 2005. A laboratory investigation of the flow in the left ventricle of a human heart with prosthetic, tilting-disk valves. Exp. Fluids 39, 322–335. https://doi.org/10.1007/s00348-005-1006-4.

Chikwe, 2018. Prosthesis type for aortic- and mitral-valve replacement. N Engl J Med 776–779. https://doi.org/10.1056/NEJMc1715189.

Van Dantzig, J.M., 1995. Doppler left ventricular flow pattern versus conventional predictors of left ventricular thrombus after acute myocardial infarction. J. Am. College Cardiol. 25, 1341–1346. https://doi.org/10.1016/0735-1097(94)00548-5.

Elbaz, M.S.M., Calkoen, E.E., Westenberg, J.J.M., et al., 2014. Vortex flow during early and late left ventricular filling in normal subjects: quantitative characterization using retrospectively-gated 4D flow cardiovascular magnetic resonance and three-dimensional vortex core analysis. J. Cardiovasc. Magn. Reson. 16, 78. https://doi.org/10.1186/s12968-014-0078-9.

Elsinga, G.E., Scarano, F., Wieneke, B., van Oudheusden, B.W., 2005. Tomographic particle image velocimetry. In: 6th Int Symp Part Image Velocim, pp. 1–12.

Falahatpisheh, A., Kheradvar, A., 2012. High-speed particle image velocimetry to assess cardiac fluid dynamics in vitro: from performance to validation. Eur J Mech B/Fluids 35, 2–8. https://doi.org/10.1016/j.euromechflu.2012.01.019.

Falahatpisheh, A., Pedrizzetti, G., Kheradvar, A., 2014. Three-dimensional reconstruction of cardiac flows based on multi-planar velocity fields. Exp. Fluids. https://doi.org/10.1007/s00348-014-1848-8.

Faludi, R., Szulik, M., D'hooge, J., et al., 2010. Left ventricular flow patterns in healthy subjects and patients with prosthetic mitral valves: an in vivo study using echocardiographic particle image velocimetry. J. Thorac. Cardiovasc. Surg. 139, 1501–1510. https://doi.org/10.1016/j.jtcvs.2009.07.060.

Fortini, S., Querzoli, G., Espa, S., Cenedese, a., 2013. Three-dimensional structure of the flow inside the left ventricle of the human heart. Exp. Fluids. https://doi.org/10.1007/s00348-013-1609-0.

Gharib, M., Rambod, E., Kheradvar, A., et al., 2006. Optimal vortex formation as an index of cardiac health. Proc. Natl. Acad. Sci. U.S.A. 103, 6305–6308. https://doi.org/10.1073/pnas.0600520103.

Goldstone, 2017. Mechanical or Biologic Prostheses for Aortic-Valve and Mitral-Valve Replacement. pp. 1847–1857. http://doi.org/10.1056/NEJMoa1613792.

Hasler, D., Landolt, A., Obrist, D., 2016. Tomographic PIV behind a prosthetic heart valve. Exp. Fluids 57, 1–13. https://doi.org/10.1007/s00348-016-2158-0.

Hasler, D., Obrist, D., 2018. Three-dimensional flow structures past a bio- prosthetic valve in an in-vitro model of the aortic root.

Hendabadi, S.A.H., Ermejo, J.A.B., Enito, Y.O.B., et al., 2013. Topology of blood transport in the human left ventricle by novel processing of doppler echocardiography. Ann. Biomed. Eng. 41, 2603–2616. https://doi.org/10.1007/s10439-013-0853-z.

Jeong, J., Hussain, F., 1995. On the identification of a vortex. J. Fluid Mech. 285, 69. https://doi.org/10.1017/S0022112095000462.

Khalafvand, S.S., Voorneveld, J.D., Muralidharan, A., et al., 2018. Assessment of human left ventricle flow using statistical shape modelling and computational fluid dynamics. J. Biomech. 74, 116–125. https://doi.org/10.1016/j.jbiomech.2018.04.030.

Khalafvand, S.S., Xu, F., Westenberg, J., et al., 2019. Intraventricular blood fl ow with a fully dynamic mitral valve model. Comput. Biol. Med. 104, 197–204. https://doi.org/10.1016/j.compbiomed.2018.11.024.

Kheradvar, A., Kasalko, J., Johnson, D., Gharib, M., 2006. An in vitro study of changing profile heights in mitral bioprostheses and their influence on flow. ASAIO J 52, 34–38.

Kilner, P.J., Yang, G., Wilkes, A.J., et al., 2000. Asymmetric redirection of flow through the heart, pp. 759–761.

Kim, W.Y., Walker, P.G., Pedersen, E.M., et al., 1995. Left ventricular blood flow patterns in normal subjects: a quantitative analysis by three-dimensional magnetic resonance velocity mapping. J. Am. Coll. Cardiol. 26, 224–238. https://doi.org/10.1016/0735-1097(95)00141-L.

Kirişli, H.A., Schaap, M., Klein, S., 2010. Evaluation of a multi-atlas based method for segmentation of cardiac CTA data: a large-scale, multicenter, and multivendor study. Am. Assoc. Phys. Med. 6279–6291. https://doi.org/10.1118/1.3512795.

Le, T.B., Sotiropoulos, F., 2012. On the three-dimensional vortical structure of early diastolic flow in a patient-specific left ventricle. Eur. J. Mech. B/Fluids 35, 20–24. https://doi.org/10.1016/j.euromechflu.2012.01.013.

Mele, D., Smarrazzo, V., Pedrizzetti, G., et al., 2018. Intracardiac flow analysis: techniques and potential clinical applications. J. Am. Soc. Echocardiogr. https://doi.org/10.1016/j.echo.2018.10.018.

Meschini, V., De, Tullio M.D., Querzoli, G., Verzicco, R., 2018. Flow structure in healthy and pathological left ventricles with natural and prosthetic mitral valves. J. Fluid Mech., 271–307 https://doi.org/10.1017/jfm.2017.725.

Metz, C.T., Baka, N., Kirisli, H., et al., 2012. Regression-based cardiac motion prediction. IEEE Trans. Med. Imaging 31, 1311–1325.

Nakashima, K., Itatani, K., Kitamura, T., Oka, N., 2017. Energy dynamics of the intraventricular vortex after mitral valve surgery. Heart Vessels. https://doi.org/10.1007/s00380-017-0967-6.

Pedrizzetti, G.I.P., Omenichini, F.E.D., Tonti, G.T., 2010. On the left ventricular vortex reversal after mitral valve replacement. Ann. Biomed. Eng. 38, 769–773. https://doi.org/10.1007/s10439-010-9928-2.

Pierrakos, O., Vlachos, P.P., Telionis, D.P., 2004. Time-resolved DPIV analysis of vortex dynamics in a left ventricular model through bileaflet mechanical and porcine heart valve prostheses. J. Biomech. Eng. 126, 714–726. https://doi.org/10.1115/1.1824124.

Querzoli, G., Fortini, S., 2010. Effect of the prosthetic mitral valve on vortex dynamics and turbulence of the left ventricular flow. Phys. Fluids. https://doi.org/10.1063/1.3371720.

Roloff, C., Stucht, D., Beuing, O., Berg, P., 2018. Comparison of intracranial aneurysm flow quantification techniques: standard PIV vs stereoscopic PIV vs tomographic PIV vs phase- contrast MRI vs CFD. J. Neurointerv. Surg. 1–8. https://doi.org/10.1136/neurintsurg-2018-013921.

Saaid, H., Segers, P., Novara, M., et al., 2018. Single calibration multiplane stereo-PIV: the effect of mitral valve orientation on three-dimensional flow in a left ventricle model. Exp. Fluids 59, 1–13. https://doi.org/10.1007/s00348-018-2504-5.

Scarano, F., 2012. Tomographic PIV: principles and practice. Meas. Sci. Technol. 24,. https://doi.org/10.1088/0957-0233/24/1/012001 012001.

Schanz, D., Gesemann, S., Schröder, A., 2016. Shake-The-Box: Lagran- gian particle tracking at high particle image densities. Exp Fluids 57, 70.

Sengupta, P.P., Burke, R., Khandheria, B.K., Belohlavek, M., 2008. Following the flow in chambers. Heart Fail Clin 4, 325–332. https://doi.org/10.1016/j.hfc.2008.02.005.

Tan, S.G.-D., Kim, S., Hon, J.K.F., Leo, H.L., 2016. A D-shaped bileaflet bioprosthesis which replicates physiological left ventricular flow patterns. PLoS One 11, e0156580. https://doi.org/10.1371/journal.pone.0156580.

Troolin, D.R., Longmire, E.K., 2010. Volumetric velocity measurements of vortex rings from inclined exits. Exp. Fluids 48, 409–420. https://doi.org/10.1007/s00348-009-0745-z.

Vraghav, V., Sudeep Sastry, N.S., 2018. Experimental assessment of flow fields associated with heart valve prostheses using particle image velocimetry (PIV): recommendations for best practices. Cardiovasc. Eng. Technol. 9, 273–287. https://doi.org/10.1007/s13239-018-0348-z.

Voorneveld, J., Muralidharan, A., Hope, T., Vos, H.J., Kruizinga, P., van der Steen, A.F. W., Gijsen, F.J.H., de Kenjeres JN BJG, S., 2018. High frame rate ultrasound particle image velocimetry for estimating high velocity flow patterns in the left ventricle. IEEE Trans. Ultrason. Ferroelectr. Freq. Control, 1. https://doi.org/10.1109/TUFFC.2017.2786340.

Vukićević, M., Fortini, S., Querzoli, G., et al., 2012. Experimental study of an asymmetric heart valve prototype. Eur. J. Mech. B/Fluids 35, 54–60. https://doi.org/10.1016/j.euromechflu.2012.01.014.

Wang, J., Gao, Q., Wei, R., Wang, J., 2017. Experimental study on the effect of an artificial cardiac valve on the left ventricular flow. Exp. Fluids 58, 126. https://doi.org/10.1007/s00348-017-2409-8.

Watanabe, H., Sugiura, S., Hisada, T., 2008. The looped heart does not save energy by maintaining the momentum of blood flowing in the ventricle. AJP Hear Circ. Physiol. 294, H2191–H2196. https://doi.org/10.1152/ajpheart.00041.2008.

Wieneke, B., 2008. Volume self-calibration for 3D particle image velocimetry. Exp. Fluids 549–556. https://doi.org/10.1007/s00348-008-0521-5.

Zang, W., Prasad, A.K., 1997. Performance evaluation of a Scheimpflug stereocamera for particle image velocimetry. Appl Opt 36, 8738–8744. https://doi.org/10.1364/AO.36.008738.